https://doi.org/10.5194/egusphere-2025-2370
Preprint. Discussion started: 6 June 2025

Seismic acquisition scheme to image overdeepened alpine valleys by high-resolution seismic method and full-waveform inversion

Thomas Burschil[1], Daniel Köhn[2], Matthias Körbe[3], Gerald Gabriel[3,4], Johannes Großmann[5], Gustav Firla[6], Markus Fiebig[6]

[1]Federal Institute for Geosciences and Natural Resources, Hannover, 30655, Germany
[2]Kiel University, Kiel, 24118, Germany
[3]LIAG Institute for Applied Geophysics, Hannover, 30655, Germany
[4]Institute of Earth System Sciences, Leibniz University, Hannover, 30655, Germany
[5]Baverian Geological Survey, Hof, 95030, Germany
[6]Department of Landscape, Water and Infrastructure, BOKU University, Vienna, 1190, Austria

Correspondence to: Thomas Burschil (thomas.burschil@bgr.de)

Abstract. The successful integration of high-resolution seismic reflection (HRSR) and full waveform inversion (FWI) enhances detailed near-surface imaging in heterogeneous glacial and post-glacial environments. To develop a tailored workflow of combining HRSR and FWI, we acquired dense P-wave and S-wave datasets, utilizing both vibratory and explosive seismic sources over an overdeepened basin in the northern Alpine foreland. The data acquisition was designed to meet the requirements of HRSR as well as FWI. Results of separated data analysis of HRSR and FWI, using standard processing workflows, show the potential of the acquired datasets. HRSR revealed detailed subsurface structures, including basin base reflectors, intra-basin discontinuities, and subtle stratigraphic variations. S-wave data provides superior resolution in imaging the basin fill down to 200 m below surface. FWI workflow converged successfully, yielding a consistent and physically reasonable model that correlates well with the HRSR results. These datasets are the basis for further methodological development of combining HRSR and FWI.

1 Introduction

Near-surface seismic methods are highly effective in subsurface imaging, i.e. in detecting stratigraphic features and geological discontinuities, but in heterogeneous environments like glacial and post-glacial deposits, seismic imaging can be challenging (Maraio et al., 2018). Nonetheless, high-resolution seismic reflection method (HRSR) provides detailed structural information by analyzing the reflected wavefield. Depending on the survey parameter, this method is often suitable to resolve the subsurface structure from depth of a few metres with a resolution in the sub-metre range down to depth of several kilometres with decreasing resolution. Utilizing S-waves instead of convenient P-waves can increase resolution even more (Pugin et al., 2009; Burschil and Buness, 2020; Pertuz and Mahlemir, 2023). However, the complexity of the subsurface is decisive for the required extent of seismic processing to ensure best imaging quality. Depending on the geological situation, true amplitude processing using common reflection surfaces as well as prestack depth migration can be superior to less enhanced processing and reveal

https://doi.org/10.5194/egusphere-2025-2370
Preprint. Discussion started: 6 June 2025

undiscovered geological features that are not observable before. Examples in the context of the investigation of overdeepened structures are allochthones Molasse blocks at the base of the sedimentary succession (Burschil et al., 2018) or cuspate-lobate folding of shallow diamict (Buness et al., 2022).

Full-waveform inversion (FWI) further fertilizes seismic imaging (Tarantola, 1986; Virieux and Operto, 2009), enabling a detailed and quantitative reconstruction of subsurface properties (e.g. Operto et al., 2013; Mecking et al, 2021; Singh et al., 2022; Beraus et al., 2024). By utilizing the entire seismic wavefield, it is possible to gain information about S-wave velocities and density distribution as well (Pan et al., 2019; Roodaki et al., 2024). However, both methods have limitations: HRSR relies on strong impedance contrasts and may struggle in complex near-surface conditions, while FWI is computationally intensive and highly sensitive to initial model accuracy. The applicability of the latter depends heavily on high-quality input data and the initial models. Despite these challenges, their combined application significantly improves geophysical interpretations in near-surface investigations. We expect an improvement in resolution, accuracy, and reliability of the data analysis.

However, HRSR and FWI set different requirements on the data. HRSR needs a broad bandwidth of the source signal to gain sharp reflections (Brodic et al., 2021). State-of-the-art FWI workflows invert the data iteratively in stages, starting with a low frequency band to avoid cycle skipping (Doktor et al., 2017; Köhn et al., 2019). These complementary prerequisites cause challenges for the data acquisition.

The scope of this paper is to demonstrate of suitable data acquisition and to create benchmark results for the combination of HRSR and FWI. We use vibratory and explosive sources to meet the different prerequisites of HRSR and FWI. We completed a P-wave survey as well as an S-wave survey that supplements the P-wave data (Burschil, 2024) and gives S-wave velocity distributions for FWI. The S-wave survey used horizontal shaking vibratory source and horizontal geophones. Study area is an overdeepened basin in the Alpine foreland, about 30 km south of Munich, Germany. It is part of a complex system of overdeepened valleys and basins that are widely spread across the European Alps (Preusser et al., 2011). This overdeepened structure is the study site 5068_3 of the ICDP project DOVE (Drilling Overdeepened Alpine Valleys; Anselmetti et al., 2021). In addition to the methodological development, the acquired data contribute to the topical research questions addressed by DOVE.

DOVE investigates glacially overdeepened structures on a pan-Alpine basis with drill-cores and geophysical surveys. The pinpoint information gained by the cores is extrapolated by the geophysical surveys to 2-D or even 3-D. Hitherto investigations focused on overdeepenings were limited to a local/regional scope. DOVE aims to gather a comprehensive picture of overdeepened structures on the scale of a whole mountain range. The core research questions to be investigated revolve around the timing and extent of Middle Pleistocene glaciations and the sedimentary dynamics associated with them. At site 5068_3,

https://doi.org/10.5194/egusphere-2025-2370
Preprint. Discussion started: 6 June 2025

the Bavarian Environmental Agency (LfU) has drilled a research borehole (5068_3_A) in 2017 and conducted a seismic refraction survey in 2018 (Großmann, priv. comm.).

2 Data acquisition strategy

Different land seismic sources are available. Each of them has certain advantages and disadvantages in emitting seismic wave. Vibratory sources are often used since they emit the energy over a certain time length. The total emitted energy accumulates but the instantaneous emitted energy is low so that the impact on the ground is low and damage to the land or infrastructure is avoided. In addition, the repeatability of emitting the same signal with the same frequency content is high (Brodic et al., 2021) and advantageous for vertical stacking to reduce incoherent noise. The peak force of a seismic vibrator refers to the maximum force output that the vibrator can exert on the ground during operation (Sallas, 1984). The emitted sweep signal with a defined frequency band is correlated with the recoded traces and produces a zero-phase Klauder-wavelet by correlation with itself (Lines and Clayton, 1977). Depending on the frequency band and the ground coupling, we emitted signal is close to the ideal, sharp Klauder-wavelet. Both advantages are complement by economic reasons, fewer regulations, and ease of approval. However, seismic vibrators are technically-limited in exciting low frequencies (Wei and Phillips, 2011). In contrast, impulsive sources emit the seismic energy instantaneously. These sources often contain a low frequency content, but depending on the emitted energy of the source, the penetration depth of seismic imaging is limited. Commonly used impulsive sources are sledgehammers, drop weight, and explosives with various charges. While sledge hammers and drop weights result in limited penetration depth, explosives deployed in boreholes are used for shallow and deep penetration (Denny and Johnson, 1991). Even peaceful nuclear explosions have been considered as seismic source (Massé, 1981). However, using explosive source is not everywhere possible, e.g. in urban areas.

On the receiver side, geophones have been used since the early 20th century to record the ground motion. Depending on the damping, the resonance frequency gives a decreasing sensitivity for lower frequencies (Krohn, 1984). Cabled systems enable a direct control of the ground motion and, thus, quality control. Autonomous systems become more and more affordable and stable so that a loss of a few percentage still enables a high fold (e.g. Manning et al., 2019; Ourabah and Chatenay, 2022). Microelectromechanical systems (Mougenot and Thorburn, 2004; Laine and Mougenot, 2014) measure the ground acceleration and are recently more deployed (e.g. Brodic et al., 2015; Gyger et al., 2025). Distributed acoustic sensing detects the strain via changes in the length of fibre optical cables. It is sensitive in the direction of the cable and strongly depends on the coupling of the cable to the ground. This rising technique has been applied in boreholes for monitoring, but also as surface receivers in telecommunication cables and fibres, deployed specially for active experiments (e.g. Jousset et al., 2018; Ziramov et al., 2022).

To meet the prerequisites and gain optimal data for combining HRSR and FWI, we deployed different seismic sources and receivers with active and passive recording techniques.

https://doi.org/10.5194/egusphere-2025-2370
Preprint. Discussion started: 6 June 2025

2.1 Seismic sources

To excite P-waves, we used the 4-ton hydraulically driven vibrator MHV4P (Fig. 1a) of the LIAG Institute for Applied Geophysics (LIAG) that has a vertical shaking unit (Burschil et al., 2021). This vibrator has a peak force of 40 kN and is limited to a lowest frequency of 20 Hz. In areas that were not accessible to vehicles, we used the electrodynamic vibrator ELVIS-7 (Wadas et al., 2016) with a vertical shaking unit (Fig. 1b). This wheelbarrow-mounted source with 1 kN peak force can be deployed along difficult paths. We set a dense source point spacing (i.e. 5 m) of doubled receiver spacing along the profile that has proven to be efficient for shallow investigations in previous studies (e.g. Tanner et al, 2015; Wadas et al., 2016; Burschil et al., 2018). Sweep frequencies were 20-200 Hz. In addition, we were able to conduct explosions using in total 1 kg charges per shot location (Fig. 1c), deployed in four 2-m deep boreholes per source point (Fig. 1d). A hydraulic breaker on a mid-sized excavator was used to push the boreholes with a 2-meter-long metal rod into the ground. We used a metal plate with a 1-by-1-m jig for positioning. For the entire acquisition, 26 explosive source points were feasible due to logistic and financial constraints. As S-wave source, we used the ELVIS-7 source with a horizontally shaking unit perpendicular to the profile direction. Nominal source point spacing was 4 m (four times receiver spacing) as a compromise to the fold and measuring process. Sweep frequency for S-waves were 20-120 Hz.

Figure 1: Seismic sources. Vibrators MHV4P (a), ELVIS-7 (b), explosives (c), and boreholes prepared for charging (d).

2.2 Receivers

For P-wave survey, we deployed 408 vertical single-component 20 Hz geophones (Fig. 2a) at 2.5 m spacing to ensure a good coverage. We chose a single spread where possible, but for one profile, we used a split-spread layout with roll-along geometry to get offset in both profile directions and a maximum offsets of at least the depth of the basin (~200 m). 24 geophones were cabled to Geometric Geodes recording units. Each Geode correlated the signal by a pilot sweep and transferred the digitized data to the recording vehicle via a wired network. In addition, 28 three-component 4.5 Hz geophones with autonomous recording units (Fig. 2b) were deployed to detect lower frequencies than the 20 Hz geophones more effectively. These geophones were placed at approximately 60 m spacing. The recording unit Omnirecs DATA-CUBE^3 has a maximum time sampling rate of 2.5 ms and an integrated anti alias filter at 80% of the sample rate (T. Ryberg, priv. comm.). For S-wave

https://doi.org/10.5194/egusphere-2025-2370
Preprint. Discussion started: 6 June 2025

survey, we used two landstreamer with 120 horizontal 10 Hz geophones, oriented perpendicular to the profile direction. We refer to these datasets on the receiver side as geode data, cube data, and S-wave data, respectively.

Figure 2: Seismic receivers. Regularly planted vertical geophones connected by cable (a), 3-component geophone and recording unit (b), and landstreamer with horizontal 1-component geophones (c).

2.3 HRSR processing

To evaluate the data for combining HRSR and FWI, we processed the vibratory source and geode data as well as the S-wave data. P-wave seismic processing was carried out in Landmark ProMAX/SeisSpace Version 5000.11.0.0 and comprised several steps: (P1) trace editing, (P2) vertical stacking for noise suppression, (P3) geometry assignment, (P4) true amplitude recovery, (P5) minimum phase transformation, (P5a) match filtering between MHV4P and ELVIS-7 source, (P6) surface consistent spike deconvolution, (P7) adaptive deconvolution (L2 norm spiking), (P8) F-K filtering for near offsets, (P9) elevation static correction, (P10) two iterations of velocity analysis in combination with residual statics, (P11) automatic gain control, (P12) normal moveout correction, (P13) common-midpoint stacking, (P14) bandpass filtering, (P15) F-X deconvolution, (P16) automatic gain control, (P17) poststack FD time migration, (P18) bandpass filtering, (P19) automatic gain control, (P20) time-to-depth conversion. Step P5a was only applied on profile SL-2P. Step P10 gives a stacking velocity field for every 25th CMP that was converted and adapted for migration (step P17) and time-to-depth conversion (step P20).

S-wave processing oriented towards the processing flow of Burschil and Buness (2020) and was carried out in Shearwater Reveal Version 6.2. The processing steps comprised (S1) trace editing, (S2) vertical stacking, (S3) geometry assignment, (S4) surface-consistent corrections in the source and receiver domains, (S5) surface-consistent deconvolution in the source and receiver domain, (S6) bandpass filtering, (S7) automatic gain control, (S8) several iterations of velocity analysis at floating datum, guided by reflectors in the stacked section, (S9) normal moveout correction, (S10) common midpoint stacking, (S11) automatic gain control, (S12) time-to-depth conversion. Step S8 gives the stacking velocities, analyzed at least every 50 m,

https://doi.org/10.5194/egusphere-2025-2370
Preprint. Discussion started: 6 June 2025

which was smoothed for time-to-depth conversion (step S12). For S-wave processing, we waived migration to reduce migration artefacts.

2.4 Full waveform-inversion

For FWI, we used the latest version of DENISE Black Edition (Köhn et al., 2012, 2014). This multiparameter FWI optimizes the P-wave and S-wave velocity using a quasi-Newton L-BFGS approach simultaneously. Input data were the explosive sources and the geode data.

As initial starting model, we created a 1-D gradient model based on first arrival analysis. From analyzing the Rayleigh surface wave, compared to the P-wave first arrivals, we infer a significant influence of damping so that we chose a visco-elastic modelling approach. To mitigate the non-linearity of the inverse problem, a sequential frequency inversion approach is applied. Six consecutive stages of low-pass filtered data with maximum corner frequencies from 7 Hz to 30 Hz were inverted. We estimated the source signature by Wiener deconvolution. Spatial smoothness constraints are implemented by an anisotropic Gaussian filter adapted to the local S-wavelength. Finally, a global correlation norm is used as objective function to mitigate source-receiver coupling effects.

3 Study site Schäftlarn

Glacially associated erosion sculpted not only the high Alpine regions but its foreland as well. The study site is located in the northern Alpine foreland that was influenced by repeated Pleistocene glaciations. About 30 km south of Munich, the former Isar-Loisach glacier lobe excavated an overdeepened structure, described by Jerz (1979) as a branch basin of the Wolfratshausen Basin to the south. The overdeepened structure is located near the town Schäftlarn at the former morphologically defined ice marginal position of the Last Glacial Maximum (LGM; Fig. 3a). The local bedrock consists of Upper-Freshwater Molasse sediments. To the west of the study site, Lake Starnberg and Lake Ammersee provide examples of overdeepenings not entirely filled by sediments. The study site is located on the southern margin of the Munich gravel plain ("Münchner Schotterebene"; Jerz, 1993). The western area of the study site is elevated approximately 100 m above the recent Isar valley incision in the East (Fig. 3b). The Molasse bedrock has been identified in outcrops at the base of the Isar valley slope (Jerz, 1987). A 198.8 m long drill-core of research borehole ICDP 5068_3_A (Fig. 3c) shows the sedimentary sequence from bottom to top: (A) ~83 m of fine-grained sediments, (B) ~111 m of coarse-grained sediments, and (C) ~4 m of diamictic sediments. Remnants of a basal diamicton could be recovered, but the bedrock was not reached (Firla et al., submitted).

At the study site, we acquired three seismic profiles with P-waves and S-waves (Fig. 3b). In the central part of profile SL-2, the path was not accessible for vehicles so we used a vertical shaking ELVIS-7 as P-wave source. The emitted energy of the smaller source is less than the energy of the MHV4P, what we directly observe in the data. At the same part of the profile, the

https://doi.org/10.5194/egusphere-2025-2370
Preprint. Discussion started: 6 June 2025

landstreamer was also not deployable so that S-wave data are not everywhere available. On SL-2, at the crossing of SL-3, the profile was also not accessible for any source, which results in a gap in the data.

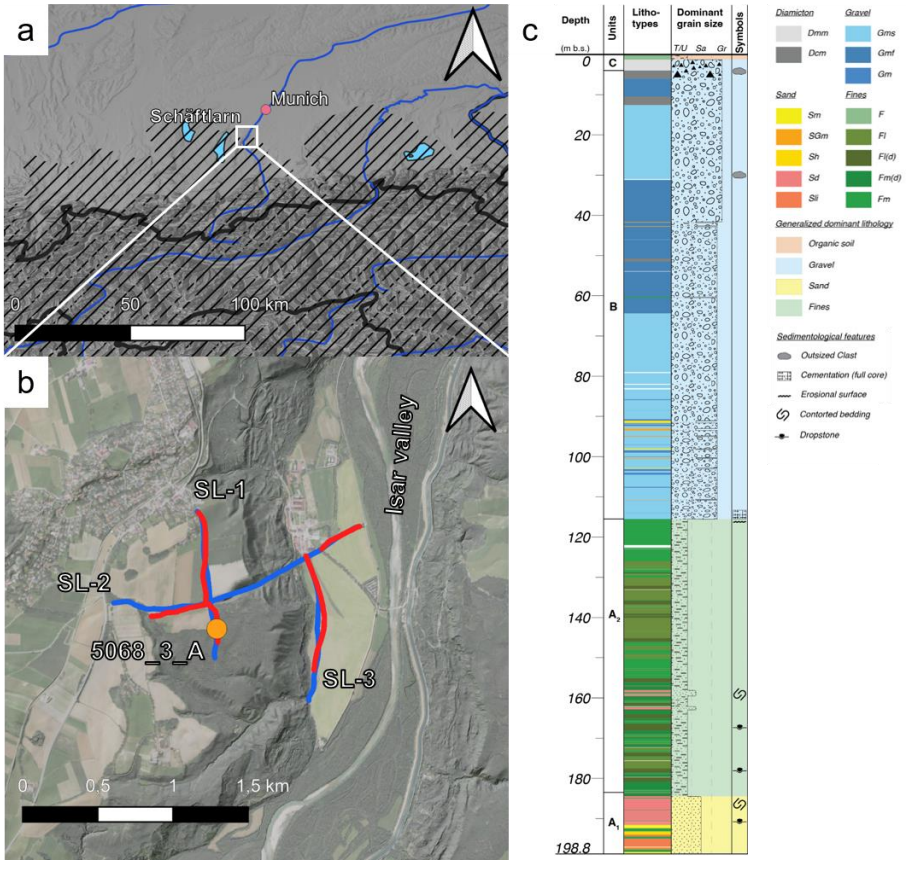

Figure 3: Study area. Overview map (a) showing the location at the rim of the LGM ice extent (hashed area; Ehlers et al., 2011) and location map (b) borehole 5068_3_A (orange) and seismic P-wave (blue) and S-wave (red) profiles. (c) Core description of borehole 5068_3_A after Firla et al. (submitted).

4 Results

4.1 Shot gathers and spectral composition

The acquired data show an excellent data quality on the various source and receiver settings (Fig. 4). Explosive sources have a good coupling and penetration depth. The dense receiver spacing of the 20 Hz geophones provide a clear first P-wave arrival, essential for generation of initial P-wave model for FWI (red arrows in Fig. 4). The explosive data show strong surface waves that are aliased in the coarse spacing of the 4.5 Hz geophones (blue arrows). The vibrator source MHV4P generated excellent

https://doi.org/10.5194/egusphere-2025-2370
Preprint. Discussion started: 6 June 2025

reflections (yellow arrows) and less surface waves than the explosive source data. An air wave arrival is also visible in the data (green arrow).

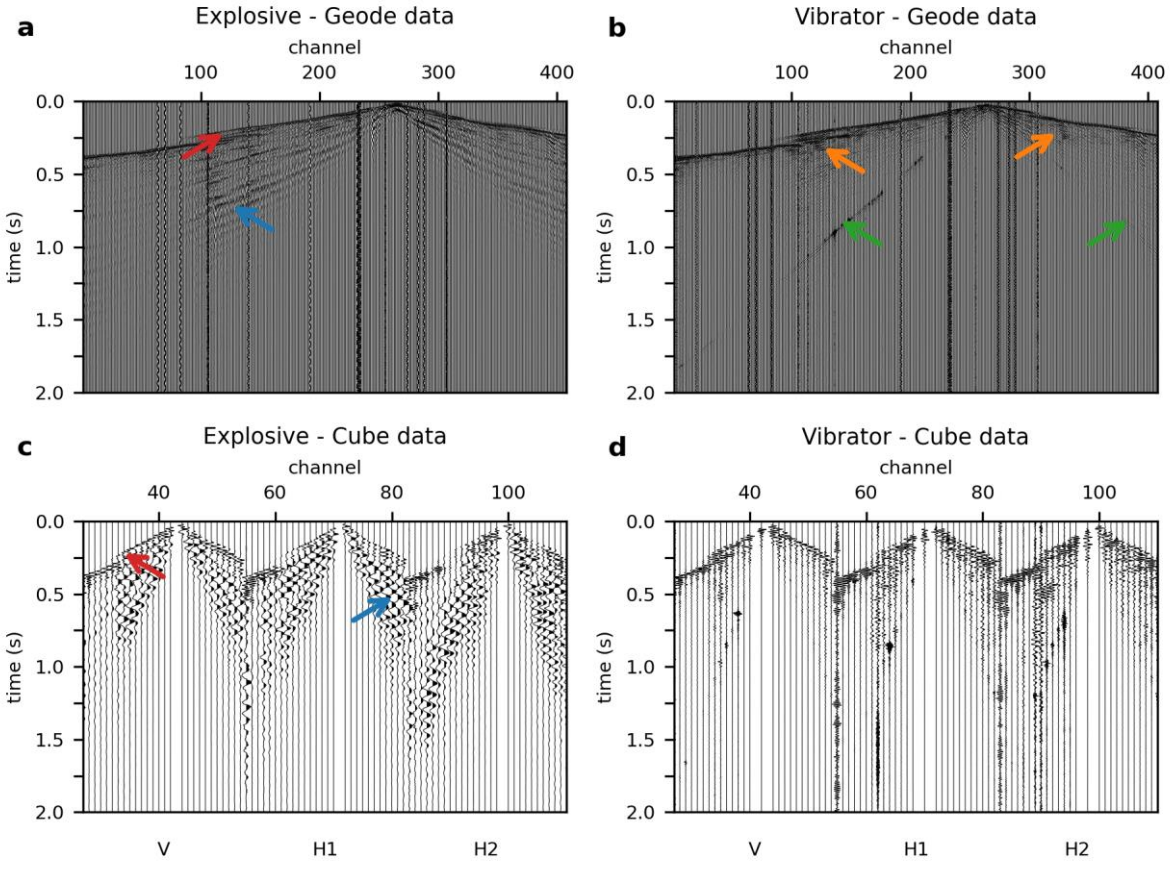

Figure 4: Source gathers for one source location (corresponding power spectral density in Fig. 5). Explosive source and 20 Hz geophones (a), vibratory source and 20 Hz geophones (b), explosive source and 3-components of 4.5 Hz geophones (c), vibratory source and 3-components of 4.5 Hz geophones (d). Note the strong surface waves (blue arrows) and the clear first arrivals (red arrows) in the explosive data, the high frequency reflections (orange arrows) in the vibratory data, as well as the air blast (green arrows).

The frequency content of the P-wave data varies across the different source and receiver configurations (Fig. 5). The source gathers of vibrator source and 20 Hz geophones show the entire sweep frequencies from 20-200 Hz. The 4.5 Hz geophones of the cube data show the same lower frequency ramp as the 20 Hz geophones, but a high cut-off frequency around 160 Hz. This cut-off is due to an anti-alias filter in the device at 80% sampling rate, i.e. 160 Hz. For the explosive sources, we detect a frequency content below 20 Hz in all data. Even the 20 Hz geophones show significant energy part below 20 Hz, the lower

https://doi.org/10.5194/egusphere-2025-2370
Preprint. Discussion started: 6 June 2025

frequency flank looks similar to the data of the 4.5 Hz geophones. However, the base level of the 4.5 Hz geophones is much lower than for the 20 Hz geophones.

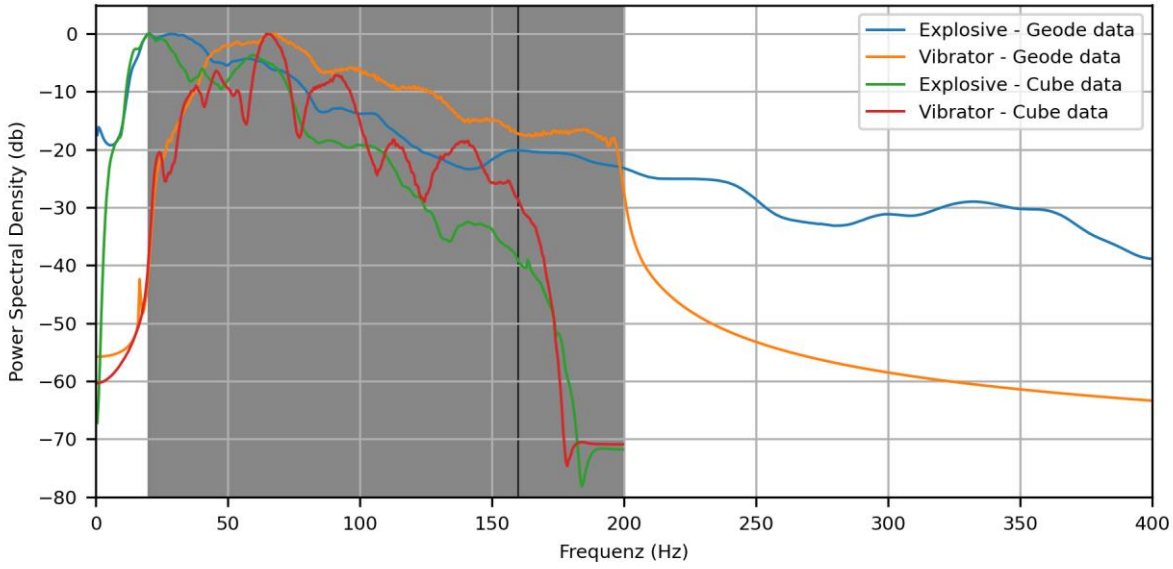

Figure 5: Power spectral density for one source gather at profile SL-1P (corresponding source gather in Fig. 4). Explosive source and 20 Hz geophones (blue), vibratory source MHV4P and 20 Hz geophones (orange), explosive source and vertical component of 4.5 Hz geophones (green), vibratory source and vertical component of 4.5 Hz geophones (red). Sweep frequency range is shaded (gray).

At the central part of SL-2P, we had to use ELVIS-7 as vibrator source. The lower peak force of the ELVIS-7 source can directly be observed. While the first arrivals can be clearly traced along the entire receiver spread for MHV4P (blue arrows in Fig. 6), the first arrivals of vibrator ELVIS-7 are only visible for offsets <250 m (orange arrows). However, both sources show a frequency content for the entire sweep from 20-200 Hz above the background noise level (Fig. 6c).

https://doi.org/10.5194/egusphere-2025-2370
Preprint. Discussion started: 6 June 2025

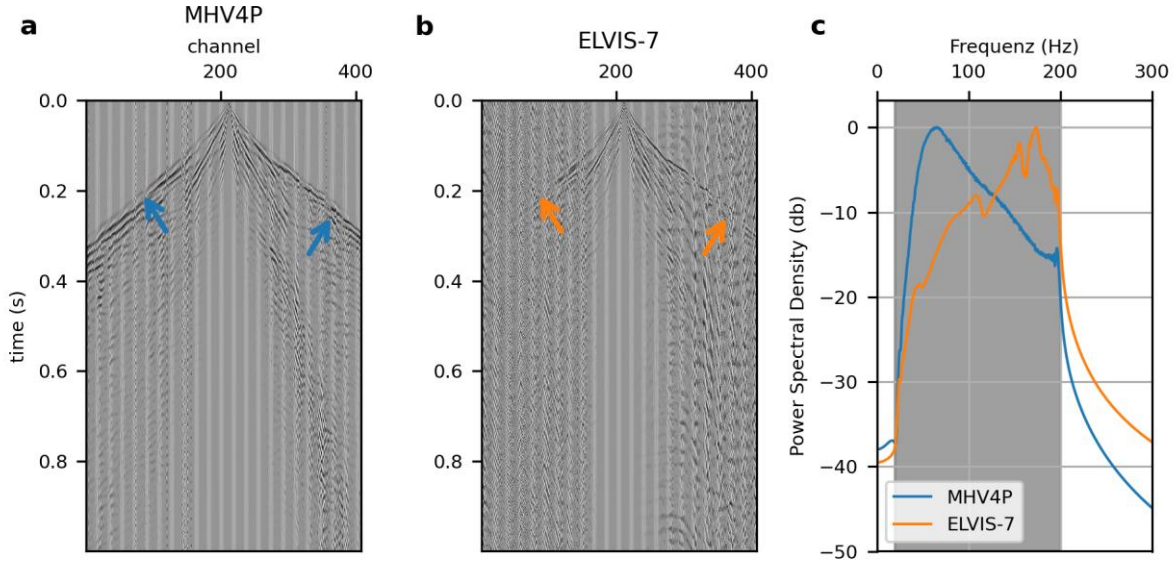

Figure 6: Source gathers for neighbouring source locations for vibrators MHV4P (a) and ELVIS-7 (b), and corresponding power spectral density for vibrators MHV4P (blue) and ELVIS-7 (orange); sweep frequency range is shaded (gray). Different source strength can be observed by first arrivals, visible for the entire profile for MHV4P (blue arrows), but not for ELVIS-7 (orange arrows).

Similar to the presented P-wave data, S-wave data show a good data quality (not shown). First arrivals and reflections can be observed on most source gather.

4.2 HRSR P-wave stacks

The newly acquired data utilizing the vibrator sources and geode data image the basin base and internal reflectors (Fig. 7). We observe deep horizontal reflectors within the Molasse (red arrows), which can also be found in the shallow region of eastern part of SL-2P (magenta arrows) and on entire profile SL-3P (not shown). Therefore, we infer that the eastern part of the study site is directly on Molasse units and here, no basin is present. We interpret strong reflectors (green arrow) as basal till at the basin base. A dipping reflector within the basin (blue arrows) separates two generations of basin fill, which was formerly not known. The log of borehole 5068_3_A (Firla et al., submitted) fits the reflectors and supports the interpretation. Unfortunately, the borehole is located only in one part of the bipartitioned basin that is separated by the dipping reflector. In the part of SL-2P, were we deployed the weaker ELVIS-7 source, we observe shallow reflections (orange arrow), but cannot trace the deeper reflectors (yellow arrows) due to less penetration. Therefore, the eastern rim of the basin, i.e. the transition of the basal basin (green arrows) towards the shallow Molasse reflectors (magenta arrows), is not imaged. The eastern profile SL-3P looks similar to the eastern end of SL-2P and is therefore not shown.

https://doi.org/10.5194/egusphere-2025-2370
Preprint. Discussion started: 6 June 2025

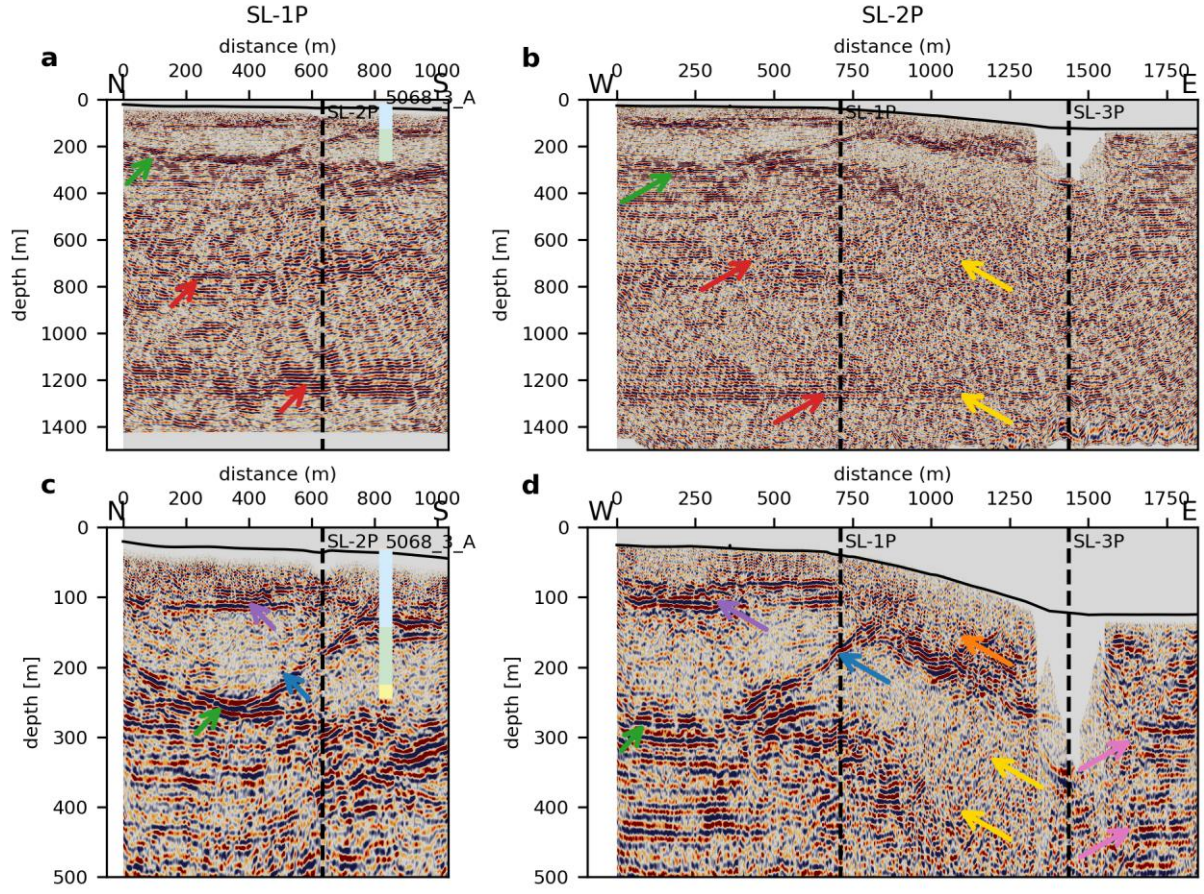

Figure 7: Migrated stacks of SL-1P (a) and SL-2P (b) and zoom to the first 500 m of the same profiles w. 1.6x vertical exaggeration (c, d). Highlighted by arrows are horizontal Molasse reflectors (red), shallow Molasse reflectors (magenta), basin base (green), basin internal reflectors (purple), discontinuity of bipartitioning (blue), area with less penetration (yellow), and transition area (orange). The log of borehole 5068_3_A shows gravel (blue), fines (green), sand (orange), and diamicton (gray).

4.3 S-wave stacks

Stacks of the S-wave data show reflections from a few ms to about 700 ms two-way traveltime, generated by a small-scale ELVIS-7 source. The sections show a similar structural image of the subsurface but with some differences (Fig. 8) compared to the P-wave images (Fig. 7):

1. The reflections are less continuous compared to the P-wave data.
2. S-wave data have less penetration depth than P-wave data.
3. S-wave data show a much higher resolution than the P-wave data.

https://doi.org/10.5194/egusphere-2025-2370
Preprint. Discussion started: 6 June 2025

In detail, we interpret a strong reflection (green arrows) as basal till at the basin base. This reflection shows an undulation that cannot be seen in the P-wave data. A reflection separates the bipartioned basin infill as seen in the P-wave data (blue arrows). This also exhibits more details than the P-wave data, but is also less continuous. A basin internal reflection is visible in the S-wave data (purple arrows) that is not present in the P-wave data. In the very shallow part, we observe a continuous reflection (red arrows) with a second reflection directly underneath (magenta arrows). Both can be seen in the P-wave data as well, but S-wave data clearly show an overlap of this reflection (magenta arrows) that is not visible in the P-wave data. The high resolution of the S-wave data enables a details interactive velocity picking.

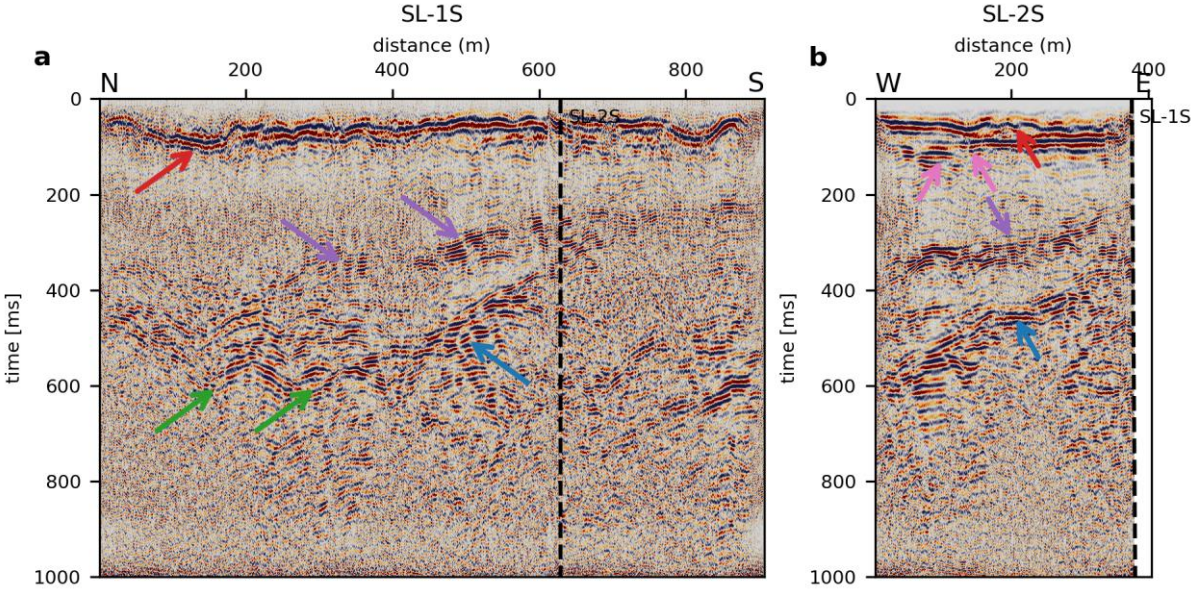

Figure 8: Stacks of SL-1S (a) and the western part of SL-2S (b). Highlighted by arrows are basin base (green), basin internal reflectors (purple), intra-basin discontinuity (blue), shallow reflections (red), and shallow discontinuity (magenta).

4.4 Full-waveform inversion

The different stages of inversion of the explosive source and geode data show a successive updating of the velocity and density distributions from the initial 1-D gradient models to the most detailed model of the last stage, inverting frequencies from 7 Hz to 30 Hz. Distributions of the last stage (Fig. 9) and changes compared to the initial model (Fig. 10) reveal the potential of FWI. The P-wave velocity distribution (Figs. 9a) reveal an undulation in the velocities (red arrows). The velocity results fits the reflectors of the stacked section (Fig. 9b; purple arrow). However, the FWI results contains details up to 30 Hz, while the stacked section contains data up to 200 Hz. In addition, the updated S-wave velocity field (Fig. 9c) and the density distribution (Fig. 9d) reveal detailed structures, even when starting from an initial 1-D gradient model.

https://doi.org/10.5194/egusphere-2025-2370
Preprint. Discussion started: 6 June 2025

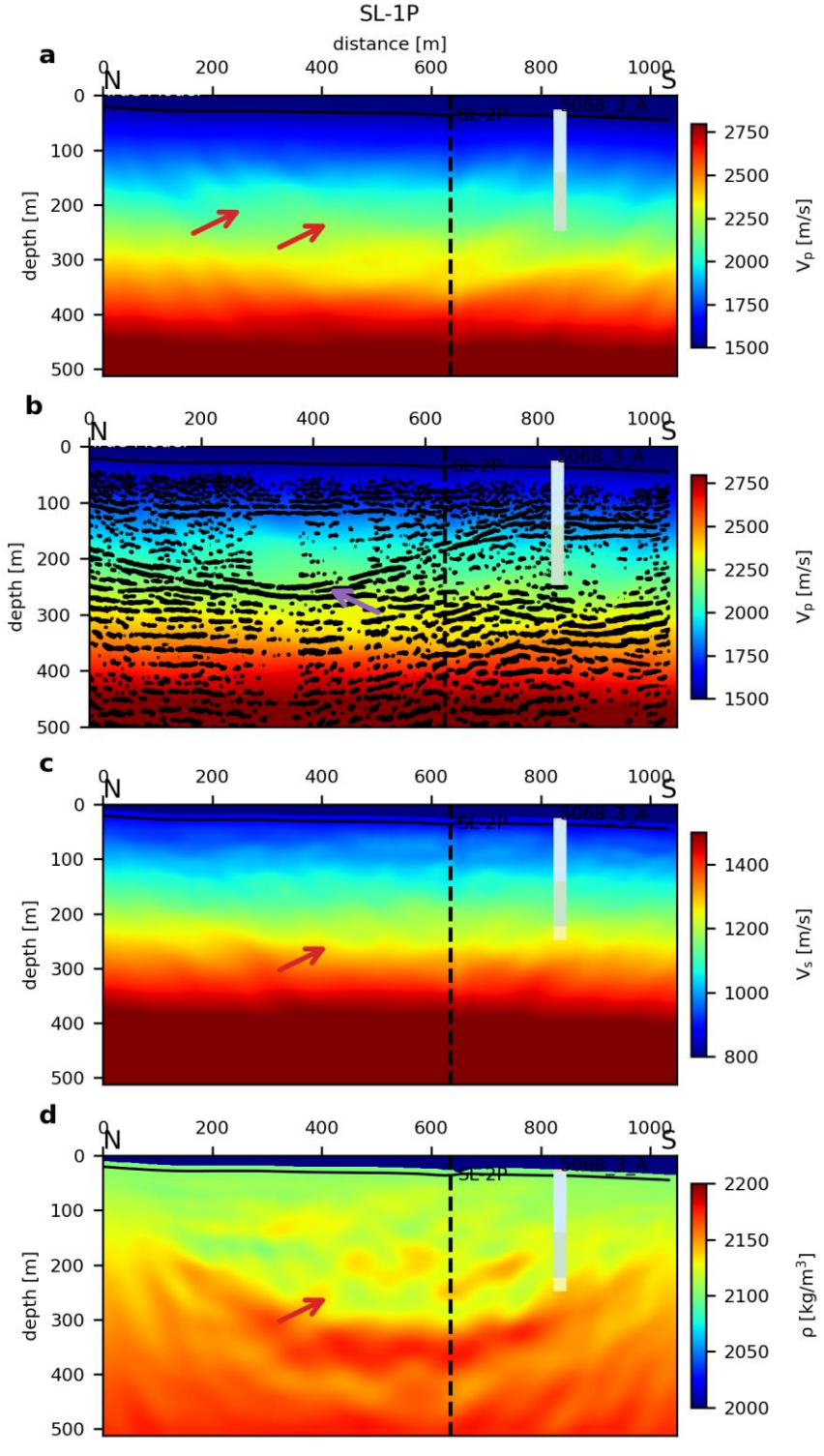

https://doi.org/10.5194/egusphere-2025-2370
Preprint. Discussion started: 6 June 2025

Figure 9: Distributions from the last stage of FWI of SL-1P for P-wave velocity (a), P-wave velocity with seismic section superimposed (b), S-wave velocity (c) and density (d). Highlighted by arrows are undulations (red arrows) and matching with reflectors in the seismic P-wave section (purple arrow).

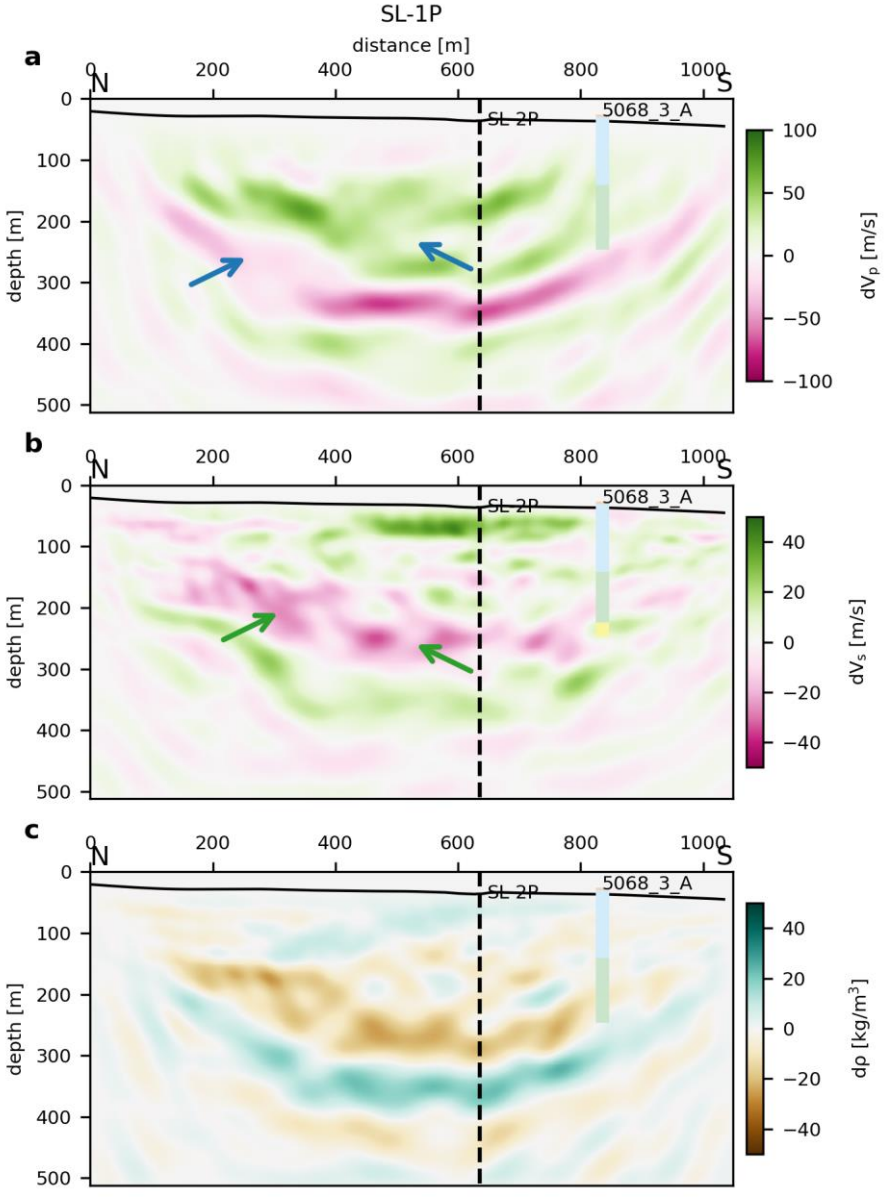

Figure 10: Change changes of the FWI of SL-1P to the initial model for P-wave velocity (a), S-wave velocity (b) and density (c). Highlighted by arrows are small-scale undulations in the S-wave velocities (green) that are not as clear in the P-wave velocities (blue).

https://doi.org/10.5194/egusphere-2025-2370
Preprint. Discussion started: 6 June 2025

5 Discussion

The dataset provides a valuable basis for developing the combination of HRSR and FWI for near-surface seismic imaging techniques. The acquired data show the contemplated frequency content and the benchmark processing reveal detailed structures of the basin to solve topical questions regarding DOVE (Firla et al., submitted).

The survey parameters were chosen to cover both requirements for HRSR as well as FWI analysis. The vibrator data show the expected bandwidth and the explosive data contains the lower frequencies. For HRSR, we used parameters that worked well in Quaternary environments in the past (e.g. Burschil et al., 2018, 2019; Buness et al, 2022). The lower sweep frequency was determined by the technical limits of the available vibrator MHV4P. We chose the upper sweep frequency (200 Hz) due to damping and thus limited benefit of higher frequencies. The charge of the explosives was specified by the blaster to avoid blowouts. This was also the reason to split the 1 kg charge in four 250 g charges per boreholes. A previous refraction survey in 2018 using 250 g did not penetrate through the gravel unit (J. Großmann, priv. comm.). P-wave receiver spacing was chosen to achieve a CMP bin size of <2.5 m to avoid aliasing, similar to Buness et al. (2022). For the cube data, we observe aliasing of the surface wave due to the wider spacing of approx. 60 m. However, since these data supplement the 2.5-m spaced dataset, we can focus on the lower frequencies.

S-wave data show a spectacular result, imaging the entire basin fill in high resolution. This is remarkable considering the small-scale source. The images reveal reflectors that were not observed in the P-wave data. The S-wave data also give a variation in the S-wave velocity distribution as basis to construct an initial model for the P-wave data. Most other studies utilize P-waves to image Quaternary sediments over decades (e.g., Hunter et al., 1984; Büker et al., 1998; Maries et al, 2017). However, other studies utilizing S-waves show also a higher resolution compared to P-waves (e.g., Pugin et al. 2009; Brodic et al., 2018; Burschil and Buness, 2020; Pertuz and Malehmir, 2023).

A preliminary interpretation of the P-wave show detailed structure within the basin fill. Our interpretation fits to the interpretation (Firla et al., submitted) at the same site. In general, the sedimentary sequence of glacial and post-glacial deposits is typical for these environments (e.g. Schaller et al., 2023; Schuster et al., 2024). The interpretation suits the reflection pattern that is similar to the seismic facies interpretation of the Tannwald Basin (Burschil et al., 2018), consisting of different lithological units.

A first attempt to use the explosive data for FWI shows the potential of FWI to image sedimentary deposits in these environments. The modeled data matches the field data without cycle skipping (Fig. 11) so that the workflow works sufficient for the acquired data. However, FWI is often applied to marine data, which often have a better signal-to-noise ratio. Sporadic other land studies show also the successful application of FWI (e.g. Köhn et al., 2012). On land, horizontally polarizied S-

https://doi.org/10.5194/egusphere-2025-2370
Preprint. Discussion started: 6 June 2025

wave data are often inverted to simplify the inversion problem (e.g. Schwardt et al., 2020; Köhn et al., 2019; Mecking et al, 2021). However, the applied inversion workflow of this study converges successfully, provides a consistent and physically reasonable solution, and matches the HRSR results.

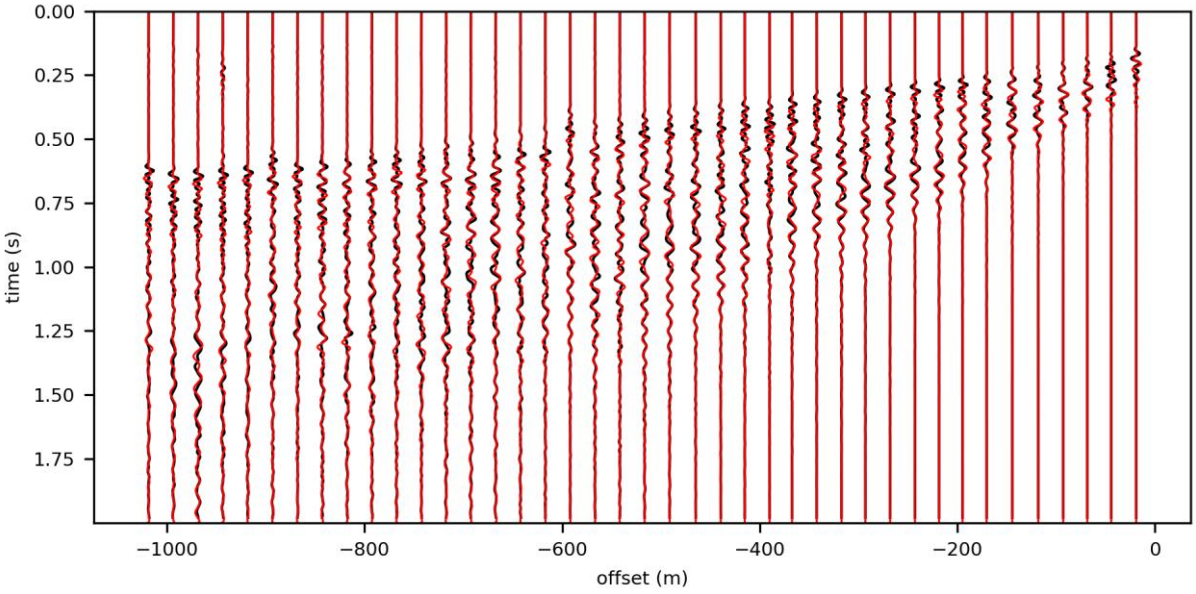

Figure 11: Example of field data and modelled data of source gather. Modelled traces match the field data.

6 Conclusions and Outlook

Both methods, HRSR and FWI, show a detailed image of near-surface geology in the complex glacially influenced environment of the overdeepened basin. Our study demonstrates that the selection and integration of different seismic sources and receiver configurations are suitable for the separate evaluation of each method. While vibrator sources with a broad frequency spectrum provide HRSR imaging, explosive sources generate low-frequency signals essential, which are for FWI. Complementary S-wave data contributed to the determination of S-wave velocities and show a superior resolution compare to P-wave data in the near surface. The acquired datasets with different sources and receivers meet the requirements for the methodological development of combining HRSR and FWI.

The HRSR images reveal a significantly improved resolution of the basin structures as well as internal reflectors, allowing for the differentiation of various sedimentation phases. S-wave data show more details within the basin infill than P-wave data. Furthermore, the dominance of the Rayleigh-wave in the field data leads to a higher sensitivity of the FWI with respect to the S-wave velocity model compared to the P-wave velocity model. To improve the resolution of the P-wave, the application of a more complex FWI workflow incorporating time-windowing of the P-waves is required. Overall, FWI results further provide

https://doi.org/10.5194/egusphere-2025-2370
Preprint. Discussion started: 6 June 2025

detailed velocity models of the sediment infill and basin geometry. This study provides valuable insights for future seismic investigations in glacially overdeepened basins and other heterogeneous geological settings.

Acknowledgment

The project Chatseis is affiliated to the ICDP project Drilling Overdeepened Alpine Valleys (DOVE) and funded by the Deutsche Forschungsgemeinschaft (DFG, German Research Foundation) – 497340281. Particular thanks to our team of BGR, LIAG, and LfU, especially the blasters Christian Veress and Brian Kröner, during the surveys as well as the support of the municipality Schäftlarn and the Monastery Schäftlarn.

Code/Data availability

Data are available under acquisition are available under doi:10.25928/960y-8w55. DENISE Black edition is available at https://github.com/daniel-koehn/DENISE-Black-Edition.

Author contribution

TB managed the project Chatseis, including fieldwork organization, data acquisition, processing of S-waves, seismic interpretation, and preparation of the manuscript. DK organized the cubes and performed FWI. MK processed the P-wave data. GG organized LIAG data, JG organized field work and explosive sources of LfU. GF and MF geological interpretation. All authors contributed to the manuscript.

Competing interests

The authors have no competing interests.

References

Anselmetti, F. S., Bavec, M., Crouzet, C., Fiebig, M., Gabriel, G., Preusser, F., and Ravazzi, C. (2022). Drilling Overdeepened Alpine Valleys (ICDP-DOVE): quantifying the age, extent, and environmental impact of Alpine glaciations. Scientific Drilling, 31, 51-70.

Beraus, S., Köhn, D., Bohlen, T., Buness, H., Burschil, T., and Gabriel, G. (2024, October). High-Resolution Shear Wave Crosshole Full-Waveform Inversion. In Third EAGE Conference on Seismic Inversion (Vol. 2024, No. 1, pp. 1-5). European Association of Geoscientists and Engineers.

Bohlen, T. (2002). Parallel 3-D viscoelastic finite difference seismic modelling. Computers and Geosciences, 28(8), 887-899.

https://doi.org/10.5194/egusphere-2025-2370
Preprint. Discussion started: 6 June 2025

Brodic, B., Malehmir, A., Juhlin, C., Dynesius, L., Bastani, M., and Palm, H. (2015). Multicomponent broadband digital-based seismic landstreamer for near-surface applications. Journal of Applied Geophysics, 123, 227-241.

Brodic, B., Ras, P., de Kunder, R., Drijkoningen, G., and Malehmir, A. (2021). Seismic imaging using an e-vib—A case study analyzing the signal properties of a seismic vibrator driven by electric linear synchronous motors. Geophysics, 86(3), B223-B235.

Brodic, B., Malehmir, A., Pugin, A., and Maries, G. (2018). Three-component seismic land streamer study of an esker architecture through S-and surface-wave imaging. Geophysics, 83(6), B339-B353.

Buness, H., Tanner, D. C., Burschil, T., Gabriel, G., and Wielandt-Schuster, U. (2022). Cuspate-lobate folding in glacial sediments revealed by a small-scale 3-D seismic survey. Journal of Applied Geophysics, 200, 104614.

Büker, F., Green, A. G., and Horstmeyer, H. (1998). Shallow seismic reflection study of a glaciated valley. Geophysics, 63(4), 1395-1407.

Burschil, T. (2024). Seismic measurements, DOVE site 5068_3 (Schäftlarn), Project Chatseis: Survey report. Federal Institute for Geosciences and Natural Resources, Hannover, Germany, 26p. http://doi.org/10.25928/pet1-6838

Burschil, T., Buness, H., and Schmelzbach, C. (2022). Near-surface three-dimensional multicomponent source and receiver S-wave survey in the Tannwald Basin, Germany: Acquisition and data processing. Near Surface Geophysics, 20(4), 331-348.

Burschil, T., and Buness, H. (2020). S-wave seismic imaging of near-surface sediments using tailored processing strategies. Journal of Applied Geophysics, 173, 103927.

Burschil, T., Buness, H., Leineweber, P., and Polom, U. (2021, August). Results of Performance Tests of Electrodynamic Vibratory Seismic Sources. In NSG2021 27th European Meeting of Environmental and Engineering Geophysics (Vol. 2021, No. 1, pp. 1-5). European Association of Geoscientists and Engineers.

Denny, M. D., and Johnson, L. R. (1991). The explosion seismic source function: Models and scaling laws reviewed. Explosion Source Phenomenology, 65, 1-24.

Dokter, E., Köhn, D., Wilken, D., De Nil, D., and Rabbel, W. (2017). Full waveform inversion of SH-and Love-wave data in near-surface prospecting. Geophysical Prospecting, 65(S1), 216-236.

Ehlers, J., Gibbard,P. L., Hughes, P. D., 2011: Quaternary Glaciations – Extent and Chronology. 1126 pp. Elsevier, Amsterdam.

Fichtner, A. (2010). Full seismic waveform modelling and inversion. Springer Science and Business Media.

Firla, G., Lüthgens, C., Burschil, T., Neuhuber, S, Schmalfuss, C., Kroemer, E., and Fiebig, M. (submitted). A MIS 8 terrestrial record retrieved from a glacially overdeepened basin in the northern foreland of the European Alps. Submitted to E&G Quaternary Science Journal.

Gyger, L., Malehmir, A., Manzi, M., Vivin, L., Lépine, J., Kaslilar, A., ... and Hamerslag, R. (2025). Broadband seismic data acquisition and processing of iron oxide deposits in Blötberget, Sweden. Geophysical Prospecting, 73(1), 80-95.

https://doi.org/10.5194/egusphere-2025-2370
Preprint. Discussion started: 6 June 2025

Hunter, J. A., Pullan, S. E., Burns, R. A., Gagne, R. M., and Good, R. L. (1984). Shallow seismic reflection mapping of the overburden-bedrock interface with the engineering seismograph—Some simple techniques. Geophysics, 49(8), 1381-1385.

Jerz, H. (1979). Das Wolfratshausener Becken: seine glaziale Anlage und Übertiefung. EandG Quaternary Science Journal, 29(1), 63-70.

Jerz, H. (1987). Geologische Karte von Bayern 1:25 000 – 8034 Starnberg Süd. Bayerisches Geologisches Landesamt, Augsburg.

Jerz, H. (1993). Das Eiszeitalter in Bayern – Erdgeschichte, Gesteine, Wasser, Boden. – Geologie von Bayern, 2, Stuttgart.

Jousset, P., Reinsch, T., Ryberg, T., Blanck, H., Clarke, A., Aghayev, R., ... and Krawczyk, C. M. (2018). Dynamic strain determination using fibre-optic cables allows imaging of seismological and structural features. Nature communications, 9(1), 2509.

Köhn, D., De Nil, D., Kurzmann, A., Przebindowska, A., and Bohlen, T. (2012). On the influence of model parametrization in elastic full waveform tomography. Geophysical Journal International, 191(1), 325-345.

Köhn D., Kurzmann A., De Nil D. and Groos L. (2014). DENISE Black Edition - User manual, available at https://danielkoehnsite.wordpress.com/software/

Köhn, D., Wilken, D., De Nil, D., Wunderlich, T., Rabbel, W., Werther, L., Schmidt, J., Zielhofer, C., and Linzen, S. (2019). Comparison of time-domain SH waveform inversion strategies based on sequential low and bandpass filtered data for improved resolution in near-surface prospecting. Journal of Applied Geophysics, 160, 69-83.

Krohn, C. E. (1984). Geophone ground coupling. Geophysics, 49(6), 722-731.

Laine, J., and Mougenot, D. (2014). A high-sensitivity MEMS-based accelerometer. The Leading Edge, 33(11), 1234-1242.

Lines, L. R., and Clayton, R. W. (1977). A new approach to vibroseis deconvolution. Geophysical prospecting, 25(3), 417-433.

Manning, T., Ablyazina, D., and Quigley, J. (2019). The nimble node—Million-channel land recording systems have arrived. The Leading Edge, 38(9), 706-714.

Maraio, S., Bruno, P. P. G., Picotti, V., Mair, V., & Brardinoni, F. (2018). High-resolution seismic imaging of debris-flow fans, alluvial valley fills and hosting bedrock geometry in Vinschgau/Val Venosta, Eastern Italian Alps. Journal of Applied Geophysics, 157, 61-72.

Maries, G., Ahokangas, E., Makinen, J., Pasanen, A., and Malehmir, A. (2017). Interlobate esker architecture and related hydrogeological features derived from a combination of high-resolution reflection seismics and refraction tomography, Virttaankangas, southwest Finland. Hydrogeology Journal, 25(3), 829-845.

Massé, R. P. (1981). Review of seismic source models for underground nuclear explosions. Bulletin of the Seismological Society of America, 71(4), 1249-1268.

https://doi.org/10.5194/egusphere-2025-2370
Preprint. Discussion started: 6 June 2025

Mecking, R., Köhn, D., Meinecke, M., and Rabbel, W. (2021). Cavity detection by SH-wave full-waveform inversion—A reflection-focused approach. Geophysics, 86(3), WA123-WA137.

Mougenot, D., and Thorburn, N. (2004). MEMS-based 3D accelerometers for land seismic acquisition: Is it time?. The Leading Edge, 23(3), 246-250.

Operto, S., Gholami, Y., Prieux, V., Ribodetti, A., Brossier, R., Métivier, L., and Virieux, J. (2013). A guided tour of multiparameter full-waveform inversion with multicomponent data: From theory to practice. The leading edge, 32(9), 1040-1054.

Ourabah, A., and Chatenay, A. (2022). Unlocking ultra-high-density seismic for CCUS applications by combining nimble nodes and agile source technologies. The Leading Edge, 41(1), 27-33.

Pan, Y., Gao, L., and Bohlen, T. (2019). High-resolution characterization of near-surface structures by surface-wave inversions: from dispersion curve to full waveform. Surveys in Geophysics, 40, 167-195.

Pan, W., Qu, L., Innanen, K. A., Dettmer, J., Macquet, M., Lawton, D., and Wang, Y. (2023). Imaging near-surface S-wave velocity and attenuation models by full-waveform inversion with distributed acoustic sensing-recorded surface waves. Geophysics, 88(1), R65-R78.

Penck, A., and Brückner, E. (1909). Bd. Die Eiszeiten in den Südalpen und im Bereich der Ostabdachung der Alpen (Vol. 3). Chr. Herm. Tauchnitz.

Pertuz, T., and Malehmir, A. (2023). Ultrahigh-resolution shear-wave reflection imaging of vertical-component data in a quick-clay prone to landslide area in southwest Sweden. Geophysics, 88(3), B121-B133.

Preusser, F., Reitner, J. M., and Schlüchter, C. (2010). Distribution, geometry, age and origin of overdeepened valleys and basins in the Alps and their foreland. Swiss Journal of Geosciences, 103, 407-426.

Pugin, A. J. M., Pullan, S. E., and Hunter, J. A. (2009). Multicomponent high-resolution seismic reflection profiling. The Leading Edge, 28(10), 1248-1261.

Roodaki, A., Janot, L., Peiro, M., Jiang, H., Gao, W., Prigent, H., ... and Kvilhaug, A. (2024). Increasing P-wave and S-wave velocity resolution with FWI—a North Sea shallow water case study. First Break, 42(5), 37-42.

Sallas, J. J. (1984). Seismic vibrator control and the downgoing P-wave. Geophysics, 49(6), 732-740.

Schaller, S., Buechi, M. W., Schuster, B., and Anselmetti, F. S. (2023). Drilling into a deep buried valley (ICDP DOVE): a 252 m long sediment succession from a glacial overdeepening in northwestern Switzerland. Scientific Drilling, 32, 27-42.

Schuster, B., Gegg, L., Schaller, S., Buechi, M. W., Tanner, D. C., Wielandt-Schuster, U., Anselmetti, F., and Preusser, F. (2024). Shaped and filled by the Rhine Glacier: the overdeepened Tannwald Basin in southwestern Germany. Scientific Drilling, 33(2), 191-206.

https://doi.org/10.5194/egusphere-2025-2370
Preprint. Discussion started: 6 June 2025

Schwardt, M., Köhn, D., Wunderlich, T., Wilken, D., Seeliger, M., Schmidts, T., Brücknet, H., Başaran, S., and Rabbel, W. (2020). Characterization of silty to fine-sandy sediments with SH waves: full waveform inversion in comparison with other geophysical methods. Near Surface Geophysics, 18(3), 217-248.

Singh, B., Malinowski, M., Górszczyk, A., Malehmir, A., Buske, S., Sito, Ł., and Marsden, P. (2022). 3D high-resolution seismic imaging of the iron oxide deposits in Ludvika (Sweden) using full-waveform inversion and reverse time migration. Solid Earth, 13(6), 1065-1085.

Sullivan, J. D. (1998). The comprehensive test ban treaty. Physics Today, 51(3), 24-29.

Tanner, D. C., Musmann, P., Wawerzinek, B., Buness, H., Krawczyk, C. M., and Thomas, R. (2015). Salt tectonics of the eastern border of the Leinetal Graben, Lower Saxony, Germany, as deduced from seismic reflection data. Interpretation, 3(3), T169-T13.

Tarantola, A. (1986). A strategy for nonlinear elastic inversion of seismic reflection data. Geophysics, 51(10), 1893-1903.

Virieux, J., and Operto, S. (2009). An overview of full-waveform inversion in exploration geophysics. Geophysics, 74(6), WCC1-WCC26.

Wadas, S. H., Polom, U., and Krawczyk, C. M. (2016). High-resolution shear-wave seismic reflection as a tool to image near-surface subrosion structures–a case study in Bad Frankenhausen, Germany. Solid Earth, 7(5), 1491-1508.

Wei, Z., and Phillips, F. (2011). Analysis of vibrator performance at low frequencies. First Break, 29(7).

Ziramov, S., Bona, A., Tertyshnikov, K., Pevzner, R., & Urosevic, M. (2022). Application of 3D optical fibre reflection seismic in challenging surface conditions. First Break, 40(8), 79-89.